Eur. Phys. J. B **11**, 469–480 (1999)

THE EUROPEAN PHYSICAL JOURNAL B

EDP Sciences

Eden growth model for aggregation of charged particles

Y.V. Ivanenko[1], N.I. Lebovka[1,2,3,a], and N.V. Vygornitskii[1]

[1] Institute of Biocolloidal Chemistry named after F.D. Ovcharenko, NAS of Ukraine, 42 blvr. Vernadskogo Kyiv 252142, Ukraine
[2] Kyiv Mogyla Academy University, 2 vul. Scovorody Kyiv 252145, Ukraine
[3] Département de Génie Chimique, DTAI, Université de Technologie de Compiègne, Centre de Recherche de Royallieu, B.P. 649, 60206 Compiègne Cedex, France

Received 2 September 1998 and Received in final form 15 January 1999

Abstract. The stochastic Eden model of charged particles aggregation in two-dimensional systems is presented. This model is governed by the following two parameters: screening length of electrostatic interaction, λ, and short-range attraction energy, E. Different patterns of finite and infinite aggregates are observed. They are of the following morphology types: linear or linear with bending, worm-like, DBM (dense-branching morphology), DBM with nucleus, and compact Eden-like. The transition between the different modes of growth is studied and phase diagram of the growth structures is obtained in λ, E co-ordinates. The detailed aggregate structure analysis, including analysis of their scaling properties, is presented. The scheme of the internal inhomogeneous structure of aggregates is proposed.

PACS. 02.70.Lq Monte Carlo and statistical methods – 36.40.Wa Charged clusters – 61.43.Hv Fractals; macroscopic aggregates (including diffusion-limited aggregates)

1 Introduction

There are a lot of computer models aimed at simulation of the natural patterns occurring in colloidal aggregation, electrochemical deposition, dielectric breakdown, bacterial colony growth, viscous fingering, spreading, etc. [1]. Such models allow to explore the process of pattern formation in real physical systems and they are based mostly on the Eden model [2] and the model of diffusion limited aggregation (DLA) [3], with the due account of particles drift, convection flow, diffusion, external field influence and specific interactions between the particles. The random successive growth (RSG) model [4], two-scale drift-diffusion model [5], diffusion-migration [6] and convection-migration models [7] are good examples of such models. They describe the most important morphology patterns observed in various non-equilibrium systems, such as DLA-like, dendritic, needle, treelike, dense-branching, compact, stingy, spiral and chiral structures [8].

Growing pattern structures and morphologies are usually controlled by the growth conditions. As an example, we may refer to a large variety of spatiotemporal patterns, which have been observed for bacterial colonies under the influence of different environmental conditions [9]. The pattern morphologies can also display the changes in interactions between the elements of growing structure or spatial extension of these interactions. The local interaction is introduced into the screened growth model [10], where the growth probability is determined by multiplicative screening contributions of the occupied sites nearest to the site of growth. Ausloos *et al.* have studied the magnetic Eden model [11] and magnetic diffusion-limited aggregation model [12] for the Izing-like nearest-neighbour interaction between the spins. Each of these models leads to formation of the different types of aggregates for different values of parameters controlling the growth processes. However, inclusion of the long-range particle interactions, for example, of dipolar type, requires considerable CPU-resources. At present, such simulations are done only for the systems of moderate size [13]. However, this question is very important for interpretation of the experimental data on magnetic particles aggregation [14].

The models of charged particles aggregation is also of a great interest. It is especially true in relation with the study of particle surface charge effects on the mechanism of colloidal aggregation [15], space charge effects in electrochemical deposition experiments [16], pattern formation mechanism in discharge systems [17] and possible fractal structure of ball lightning [18]. The presence of the long-range interactions can produce the qualitatively new effects, not usual for the systems with the short-range interactions. Recently, unusual chiral growth patterns were observed for the two-dimensional electrostatic model [19]. The authors have shown using both experimental and simulation evidences that this chirality results from existence of the long-ranged interactions between the charged growing branches and can even exist in the absence of any microscopic chirality. The limited stability of systems

[a] e-mail: lebovka@roller.ukma.kiev.ua

with the spatial charge distribution is their another interesting feature. It is well known that the electrostatic interactions cause the loss of stability of a charged droplet [20] and may cause instabilities of charged polymer systems [21], aerosols [22], etc. Under the non-equilibrium growth condition one may expect occurrence of such phenomena as large-scale fluctuations, lacunarity or growth of finite size aggregates.

In this work, we propose the stochastic Eden-like lattice model of charged particles aggregation. Particles overcome the electrostatic repulsive barrier created by the aggregate and stick to it due to existence of a short-range attraction force. We observe formation of the aggregates with the following different morphologies: linear or near-linear, linear with bending, worm-like, DBM or DBM with nucleus, and compact Eden-like. The transition between the different modes of growth is governed by the two model parameters: screening length, λ, and attraction energy, E. This model is the natural extension of RSG model [4], which was used for explanation of the two-dimensional pattern formation in the processes of metal-semiconductor films crystallisation and of bacterial colony growth. We consider the more general case of long-range interparticle repulsions of type $u \sim 1/r$, whereas the RSG model corresponds to the case when interparticle repulsion energy u does not depend on interparticle distance r, *i.e.*, $u = \text{const}$.

The structure of the paper is as follows. In Section 2 we describe the model. Section 3 reports the results of simulation and their discussion, including examples of the clusters, phase diagram, analysis of the radial cluster structures and their scaling properties. Section 4 contains our conclusions. Appendix A presents some simple electrostatic estimations for the model.

2 Model

The model is based on the standard 2d stochastic Eden model [2]. We assume that all the particles bear the same electric charge q. A particle located at the point j in the proximity of the aggregate interacts with all the particles of aggregate through the long-range Coulomb repulsion, $U > 0$, and short-range "glue" attraction, E. We also take into account the possibility of electrostatic repulsion screening and introduce the screening length λ, in order to switch off the influence of the aggregate particles located farther then at the distance λ from the point j. The energy of electrostatic repulsion may be defined as:

$$U(j) = \sum_i q^2 a_{ij}/r_{ij}, \tag{1}$$

where r_{ij} is a distance between the j-point and the i-particle of the aggregate, $a_{ij} = 1$ for $r_{ij} < \lambda$ and $a_{ij} = 0$ in any other cases. The cluster growth takes place on the simple square lattice. The lattice step and the particle charge are assumed to be equal to 1. So, in this model, the cluster growth is governed by two parameters: the screening length, λ, and the attraction energy, E, and we may consider the values of λ, U and E as dimensionless.

A cluster grows according to the following scheme:

a) the seed particle of the cluster is placed at the lattice point $x = y = 0$;

b) the cluster perimeter site, j, is chosen randomly (the perimeter of the cluster is a set of unoccupied lattice sites nearest to the cluster); the value of U for the j-site is calculated and compared with the E-value;

c) if $U \leq E$, then the j-site becomes the site of a cluster, and determination of a new cluster perimeter site takes place; otherwise, if $U > E$, the j-site is declared as unoccupied forever;

d) then the step b) is reiterated.

These steps run until the cluster reaches either the lattice edge, or the desirable size, or until the cluster growth termination. The last case may be observed when the following condition becomes true for all the sites of cluster perimeter:

$$U > E. \tag{2}$$

The lattice size varied from 300×300 to 5000×5000, the maximal number of particles in the cluster did not exceed 3×10^5. As a rule, we averaged the results over the 10–50 different realisations.

3 Results and discussions

3.1 Phase diagram

Figure 1 presents examples of clusters that appear at different values of the screening length, λ, and attraction energy, E. All patterns were obtained on the basis of cluster images on 400×400 lattice. Small circle in the centre of each pattern denotes the seed particle. The plane of λ and E values is approximately divided into several regions that correspond to the observed cluster types. These regions are schematically presented on the phase diagram in Figure 2. The numbers of patterns of the Figure 1 correspond to the numbers of the black squares put on the phase diagram. We discern the following regions of the phase diagram:

$\mathbf{L_f}$ is the region of linear or near-linear finite cluster growth;

$\mathbf{Lb}_\infty$ is the region of infinite linear clusters or linear clusters with bending;

$\mathbf{W_f}$ is the region of finite worm-like clusters; this type of structure is represented by the patterns 1, 5, 9, 13 of Figure 1 and similar structures are reported to occur for the random successive growth model [4];

$\mathbf{W}_\infty$ is the region of infinite worm-like clusters; this structure type examples are presented by the patterns 2, 3, 6, 7, 10, 14 of Figure 1;

$\mathbf{DB}_\infty$ is the region of lacunary clusters, clusters with developed branch structure and clusters of DBM–type [8] structure growth; in this region, clusters may possess

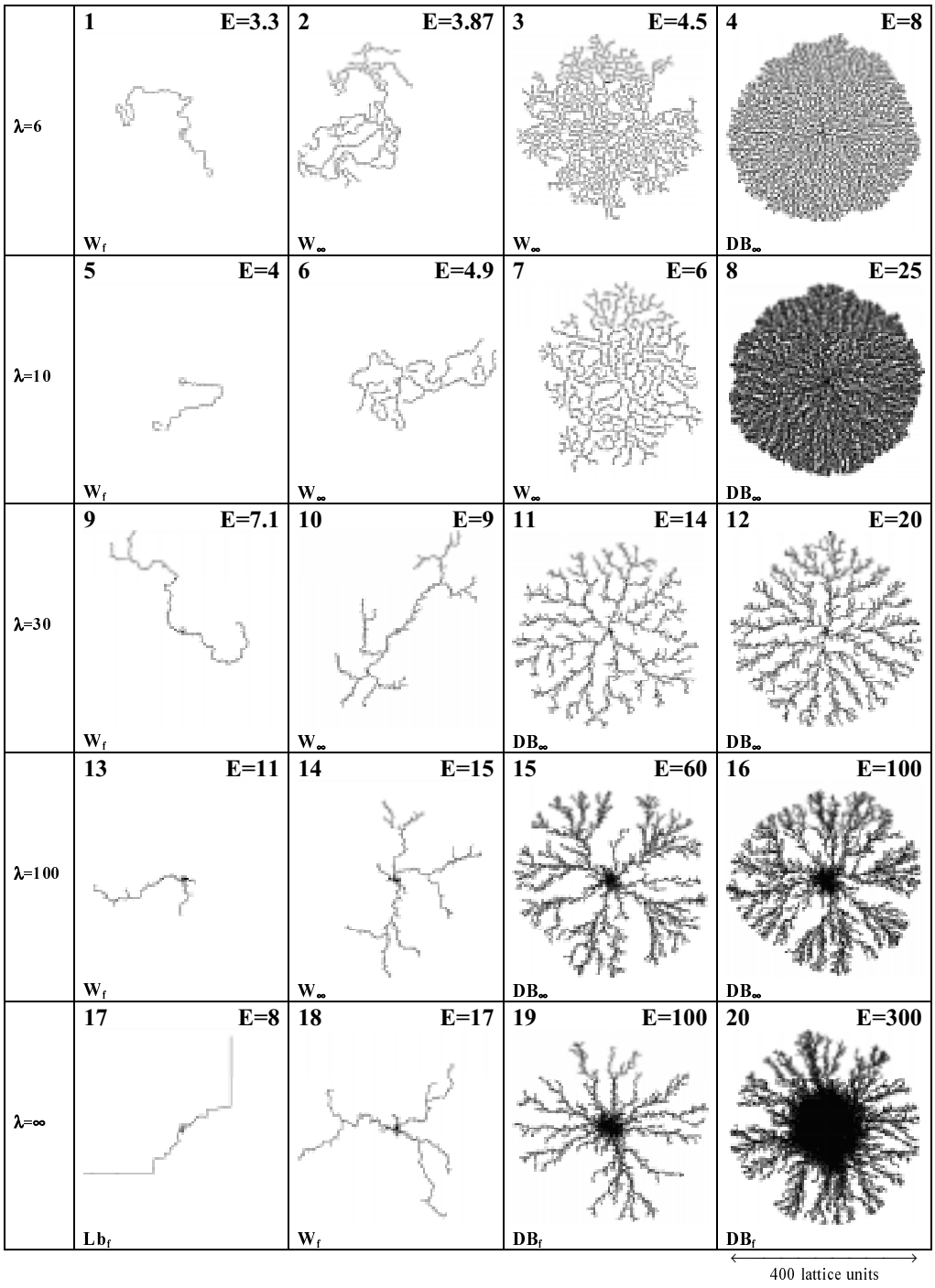

Fig. 1. Examples of cluster patterns at different values of the attraction energy E and screening length λ. Numbers of patterns correspond to the numbered black squares on the phase diagram in Figure 2. All patterns are displayed on the same scale 400×400. The cluster growth stops when it reaches the edge of the lattice.

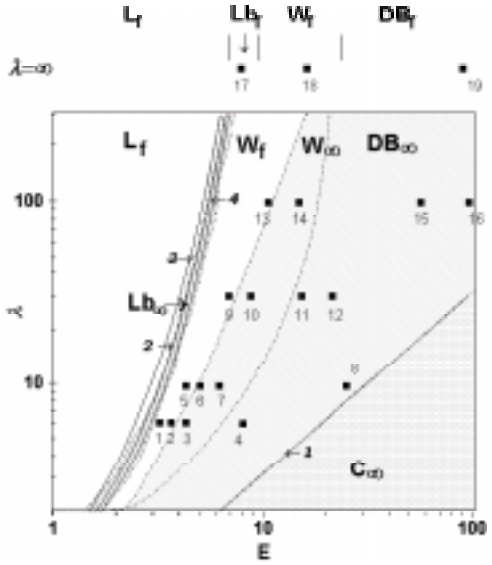

Fig. 2. Phase diagram for the cluster growth in co-ordinates of screening length λ *versus* attraction energy E. Here, lines 1,2,3 and 4 are derived from equations (A.6, 10, 5) and (12), respectively. See the text for other details.

a central dense part or a nucleus (see, patterns 4, 8, 11, 12, 15, 16 of Fig. 1);

$\mathbf{C}_\infty$ is the region of compact clusters or compact clusters with cavities growth; in the limit of $E \to \infty$ these clusters are the clusters of a standard Eden model.

The case of $\lambda = \infty$ (see 17-20, Fig. 1) is shown above the main diagram (Fig. 2). There are no regions of infinite cluster growth and no compact cluster growth for $\lambda = \infty$ (except for the limiting case of $E = \infty$, when the growth of the Eden-like clusters takes place).

Thus, on increasing of E at fixed λ value, we observe the following sequences of regions

$$\mathbf{L_f} \to \mathbf{Lb}_\infty \to \mathbf{W_f} \to \mathbf{W}_\infty \to \mathbf{DB}_\infty \to \mathbf{C}_\infty \qquad (3)$$

when λ is finite, and

$$\mathbf{L_f} \to \mathbf{Lb_f} \to \mathbf{W_f} \to \mathbf{DB_f} \qquad (4)$$

when $\lambda = \infty$.

The main distinctive feature of the phase diagram in Figure 2 is the existence of regions with *finite* and *infinite* cluster growth. It appears merely due to the long-range character of Coulomb interactions. When a cluster grows, its total charge increases and it results in increase of the electrostatic repulsion energy at the points of new particle attachment, which are located on the cluster perimeter. In certain cases, when the cluster grows sufficiently large, the condition of cluster growth termination (2) realises for all the points of cluster perimeter. We characterise the maximal size of a cluster by its maximal radius $R_{\max}$, which is simply the distance from the central seed particle to the most remote particle of the cluster. The full manifestation of the long-range character of Coulomb interactions occurs only in the cases when the value of λ exceeds the

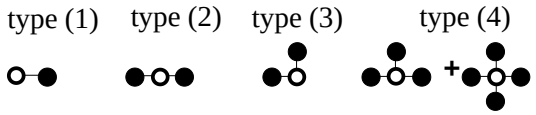

Fig. 3. The four types of the nearest neighbour configurations of cluster growing on a square lattice discerned for the purposes of configuration analysis.

spatial dimension of the cluster, *i.e.* when $\lambda \geq R_{\max}$. This condition is always true when $\lambda = \infty$, which is the cause of only finite cluster growth.

How is it possible to discern the different regions of the phase diagram presented in Figure 2? Some conclusions about localisation of different regions can be made on the base of the visual analysis of patterns similar to that presented in Figure 1. For fixed λ, the increase of E leads to the growth of different type of clusters. Thus, in $\mathbf{L_f}$ region the length of cluster increases with E and in $\mathbf{Lb}_{\mathbf{f}(\infty)}$ region the number of cluster bendings increases and the length of the linear cluster part decreases with the increase of E. However, the visual analysis does not allow us to make an exact estimation of region localisations. This method is effective only for determination of the sharp boundary between the region $\mathbf{DB}_\infty$ and region $\mathbf{C}_\infty$. Note that this boundary can be also localised by the means of simple electrostatic estimations (See Appendix) and line 1 in Figure 2 is derived from equation (A.6).

The boundaries of $\mathbf{L_f}$, $\mathbf{Lb}_\infty$, $\mathbf{W_f}$ and $\mathbf{W}_\infty$ regions are not defined clearly and the transition from one phase to another is not sharp and appears to be rather smeared. Due to the finite-size effects near the boundaries of regions, we observe strong fluctuations of cluster sizes and morphologies. The width of these transition zones between the different regions may vary and it is difficult to determine it precisely, however, in our simulations it does not exceed $\Delta E \approx 0.2$ for fixed λ. On moving from region $\mathbf{L_f}$ to region $\mathbf{Lb}_\infty$ at fixed λ value, the closer we are to region $\mathbf{Lb}_\infty$, the higher is the probability of an infinite linear cluster growth. Correspondingly, the probability of the finite linear cluster growth becomes lower. For estimation purposes, the boundary line may be defined as a line of approximately equal probabilities of infinite and finite cluster formation. This is true also for the cases of $\mathbf{Lb}_\infty - \mathbf{W_f}$ and $\mathbf{W_f} - \mathbf{W}_\infty$ boundaries. Unfortunately, this approach is not acceptable for the case of boundary localisation between $\mathbf{W}_\infty$ and $\mathbf{DB}_\infty$ regions.

To estimate the region boundaries more precisely, we have carried out the configuration analysis of cluster structures and have studied the behaviour of the maximal cluster radius $R_{\max}$ and of its centre of mass displacement $\Delta R_{\rm c}$.

3.2 Configuration analysis, maximal cluster radius and its centre of mass displacement

The transitions between the different regions of a phase diagram may be also analysed with the help of configuration analysis. The idea is to find some correlation between the type of a pattern and the probability of a certain nearest neighbour configuration in that pattern. Any cluster

on a simple square lattice consists of the particles that have 1, 2, 3 and 4 nearest neighbours. For the purposes of configuration analysis, we discern four types of configurations presented in Figure 3.

It is easy to see that the configurations of type (1) correspond to the points of cluster growth termination, the linear clusters consist mostly of type (2) linear configurations, the clusters with bending and worm-like clusters are the mixtures of type (2) and type (3) configurations of particles and the particles of compact and branched clusters form mostly configurations of a type (4).

The fractions of particles in (i) type configurations, P_i, were calculated as the ratios of particles having one neighbour in configuration (1), two neighbours in configuration (2), two neighbours in configuration (3) and three or four neighbours in configuration (4), respectively, to the total number of cluster particles.

To localise more precisely the boundary between the above mentioned finite and infinite cluster regions, we have also studied the dependency of the maximal cluster radius $R_{\max}$ *versus* attraction energy E for fixed values of screening length λ. The results were averaged over $10-30$ different initialisations for each chosen pair of values λ, E and the maximal lattice size used in this work was 5000×5000. A cluster reaching the lattice boundaries was considered as infinite. Such clusters were observed only for $\lambda<\infty$, while, as it is mentioned above, for $\lambda=\infty$ all clusters are only finite, they stop to grow far beyond the limits of our system.

Figures 4, 5 show the fractions of particles with relevant nearest neighbour configurations, P_i (a) and the maximal cluster radius, $R_{\max}$ *versus* E (b) for $\lambda=30,\infty$, respectively. These figures correspond to the continuous movement along the E axis across the phase diagram presented at Figure 2 at fixed values of λ.

Note that at finite λ the transition between the finite and infinite growth regions in the sequence (3) is obvious at $R_{\max}$ *versus* E curve (Fig. 4b). This is the way to fix the transition boundaries between the $\mathbf{L_f}$–$\mathbf{Lb}_\infty$, $\mathbf{Lb}_\infty$–$\mathbf{W_f}$, or $\mathbf{W_f}$–$\mathbf{W}_\infty$ regions quite reliably.

In the region of linear or near-linear finite cluster growth ($\mathbf{L_f}$) the considerable increase of P_2, is observed with E increase with relatively weak P_1, P_3 and P_4, *vs.* E dependencies. This P_2 increase is accompanied by the increase of $R_{\max}$. The $\mathbf{L}_\mathrm{f}$–$\mathbf{Lb}_\infty$ boundaries (for $\lambda=30$, Fig. 4) or $\mathbf{L_f}$–$\mathbf{Lb_f}$ boundaries (for $\lambda=\infty$, Fig. 5) at $E=E_\mathrm{b}(\lambda)=E_{\mathbf{L_f}-\mathbf{Lb}_\infty(\mathbf{L_f}-\mathbf{Lb_f})}$ approximately correspond to the region of maximal P_2 values.

We can estimate the $R_{\max}(E)$ dependence in the $\mathbf{L_f}$ region, as well as the $E=E_\mathrm{b}(\lambda)$ boundary between the $\mathbf{L_f}$ and $\mathbf{Lb}_\infty$ regions (at finite λ) proceeding from the following electrostatic considerations. The mainly linear clusters grow at small values of E in the $\mathbf{L_f}$ region. The particles in this region tend to join the chain cluster at the tips where the repulsive energy U is the lowest. The particles forming a linear chain of a length L, repulse the newcomer at the edge of the chain with the

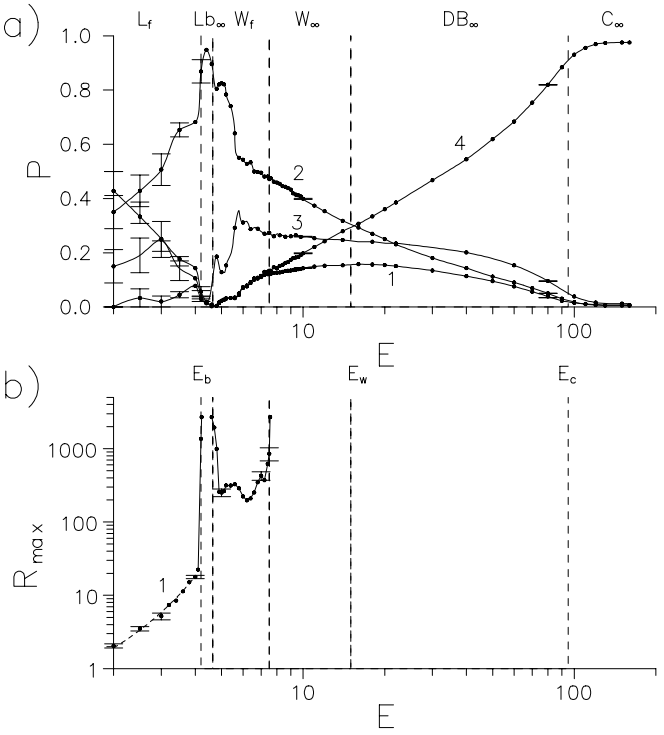

Fig. 4. The fractions of different types of particle configurations, $P_i, i=1/4$ (a), and maximal cluster radius, $R_{\max}$,(b) *versus* attraction energy, E, at $\lambda=30$. The value of E_b determines the boundary between the $\mathbf{L_f}$ and $\mathbf{Lb}_\infty$ regions and may be approximated by equation (10). The value of E_w determines the boundary between the $\mathbf{W}_\infty$ and $\mathbf{Db}_\infty$ regions. The value of E_c determines the boundary between the $\mathbf{DB}_\infty$ and $\mathbf{C}_\infty$ regions and may be approximated by equation (9). The dashed portion of the curve corresponds to the $R_{\max}(E)$ curve in the interval of $E<E_\mathrm{b}$ obtained through rms approximation using equation (9).

energy $U=U_{\mathrm{lin}}$ (Fig. 6):

$$U_{\mathrm{lin}}=U_{\mathrm{lin}}(\lambda)=\sum_{r=1}^{\lambda}\frac{1}{r}=\psi\left(\lambda+1\right)+C, \tag{5}$$

where $\psi\left(\lambda+1\right)$ is the Psi function and

$$C=\lim_{\lambda\to\infty}\left(\sum_{r=1}^{\lambda}\frac{1}{r}-\ln\lambda\right)=0.577216... \tag{6}$$

is the Euler constant [24].

In the case, when $\lambda\gg1$ we obtain from (5)

$$U_{\mathrm{lin}}(\lambda)\simeq\int_1^{\lambda}\frac{\mathrm{d}r}{r}=\ln\lambda, \tag{7}$$

for all finite $\lambda\leq L$, and

$$U_{\mathrm{lin}}\simeq\ln(L), \tag{8}$$

when $\lambda>L$ or $\lambda=\infty$.

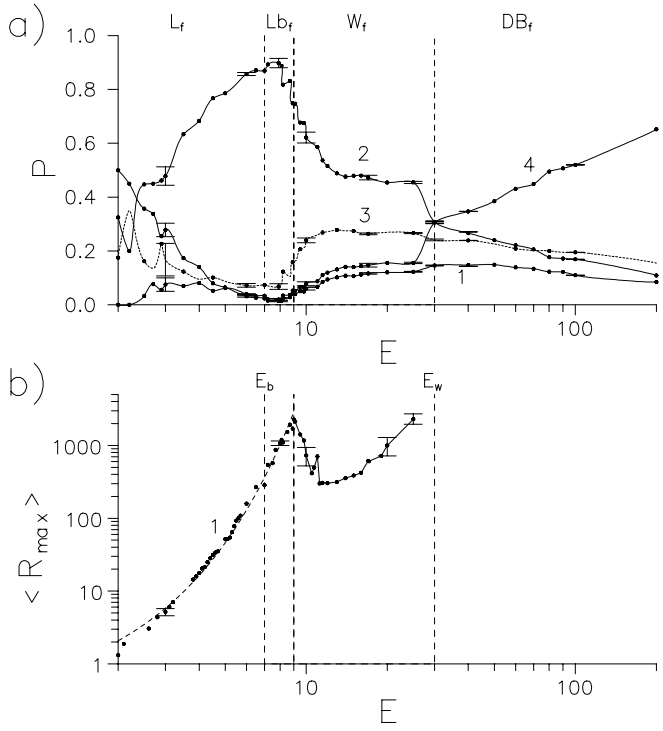

Fig. 5. The fractions of different types of particle configurations, $P_i, i = 1/4$ (a), and maximal cluster radius, $R_{\max}$, (b) *versus* attraction energy, E, at $\lambda = \infty$. The value of $E_{\rm b}(\approx 8)$ determines the boundary between the $\mathbf{L_f}$ and $\mathbf{Lb_f}$ regions. The value of $E_{\rm w}$ determines the boundary between the $\mathbf{W_f}$ and $\mathbf{Db}_{\rm f}$ regions. The dashed portion of the curve corresponds to the $R_{\max}(E)$ curve in the interval of $E < E_{\rm b}$ obtained through rms approximation using equation (9).

The growth of the linear chain terminates when the cluster growth termination condition (2) gets realised, so that we have for the maximal radius at $E < E_{\rm b}(\lambda)$:

$$R_{\max} \propto \exp(E), \tag{9}$$

where, the $E_{\rm b}(\lambda)$ dependency may be approximated for finite $\lambda(\lambda < 200)$ by

$$E_{\rm b}(\lambda) \cong \ln(\lambda) + 0.922, \tag{10}$$

which corresponds to the boundary line between the $\mathbf{L}_{\rm f}$ and $\mathbf{Lb}_\infty$ regions (See Fig. 2, line 2) and $E_{\rm b}(\lambda = \infty) \cong 8.0$ is the boundary line between the $\mathbf{L_f}$ and $\mathbf{Lb_f}$ regions.

At any λ value the equation (9) approximates quite well the behaviour of $R_{\max}(E)$ in the interval of $E < E_{\rm b}(\lambda)$ (see Figs. 4b–5b).

We note that the phase of infinite growth $\mathbf{Lb}_\infty$ exists between the two finite growth phases. It is possible to understand the cause of such surprising behaviour using the following considerations. For the purely linear mode

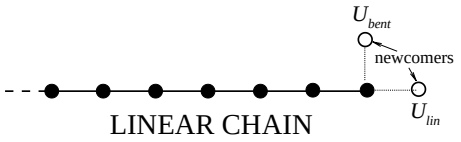

Fig. 6. The possible newcomers at the edge of linear chain with repulsive energies of $U_{\rm lin}$ (see Eq. (5)) for linear configuration of type (2) (Fig. 3) and $U_{\rm bend}$ (see Eq. (12)) for bent configuration of type (3) (Fig. 3).

of growth the increase of E at fixed finite λ results in transition of $\mathbf{L}_{\rm f} \to \mathbf{Lb}_\infty$, when

$$E \approx U_{\rm lin}(\lambda) \simeq E_{\rm b}(\lambda). \tag{11}$$

On further increase of E, the bent configurations of type (3) (Fig. 3) can appear effectively. In this case, the particles forming a linear chain repulse the newcomer at the edge of the chain with the energy $U = U_{\rm bend}$ (Fig. 6):

$$U_{\rm bend}(\lambda) = \sum_{r=1}^{\lambda} \frac{1}{\sqrt{1 + (r-1)^2}}, \tag{12}$$

and in the case, when $\lambda \gg 1$ we have

$$U_{\rm bend}(\lambda) \simeq \int_1^{\lambda} \frac{{\rm d}r}{\sqrt{1 + (r-1)^2}} \simeq \ln 2\lambda. \tag{13}$$

At higher E ($E > U_{\rm bend}$) the linear chains of cluster begin to destroy and its structure becomes more compact. In this case, the transition condition (11) is not true any more and, as a result, we observe the backward transition to re-entrant phase of finite growth $\mathbf{W}_{\rm f}$.

So, we can approximate the existence range of $\mathbf{Lb}_\infty$ phase by the following bounds on E at fixed λ:

$$U_{\rm lin}(\lambda) \lesssim E \lesssim U_{\rm bend}(\lambda), \tag{14}$$

and lines 3 and 4 shown on the phase diagram (Fig. 2) correspond to these bounds.

The transition to the $\mathbf{W}_{\rm f}$ region, where the growth of finite worm-like clusters takes place (both for $\lambda = 30$ and for $\lambda = \infty$), is accompanied by the sharp decrease of $R_{\max}$ with the simultaneous increase of the fraction of the particles forming type (3) configurations, P_3.

We approximately localise the boundaries $\mathbf{W}_\infty - \mathbf{DB}_\infty$ (for finite λ) or $\mathbf{W_f} - \mathbf{DB_f}$ (for $\lambda = \infty$) at those values of $E = E_{\rm w} = E_{\mathbf{W}_\infty - \mathbf{DB}_\infty(\mathbf{W_f} - \mathbf{DB_f})}$, which correspond to the transition to the radial-symmetrical mode of growth. The distinctive feature of patterns obtained at $E > E_{\rm w}$ is their obviously radial structure (see the patterns presented in Fig. 1), the existence of a dense part or nucleus centred on the seed particle and observance of the maximal growth velocity mainly in the radial direction outward from the nucleus. At lower energies, the linear or worm-like clusters do not display such obviously radial structures and the cluster centre can no longer coincides with the seed particle.

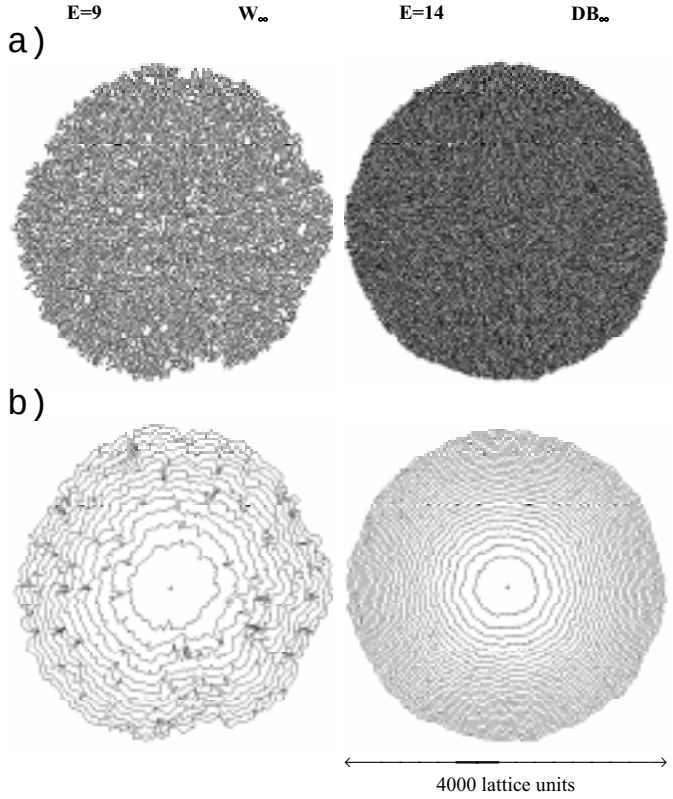

Fig. 7. Patterns (a) and time snapshots of the interface evolution (b) for the $\mathbf{W}_\infty$ – cluster and $\mathbf{DB}_\infty$ – cluster at $\lambda = 30$ and for the $E = 9$ and $E = 14$, respectively. These are the same clusters as those shown as 10 and 11 in Figure 1, but they were grown at the larger scale lattice of 4000×4000 dimension. Time snapshots correspond to the growth interfaces at each next 5×10^4 attached particles. Particles at the growth interface are connected by the straight lines. Cross in the centre corresponds to the seed particle localisation.

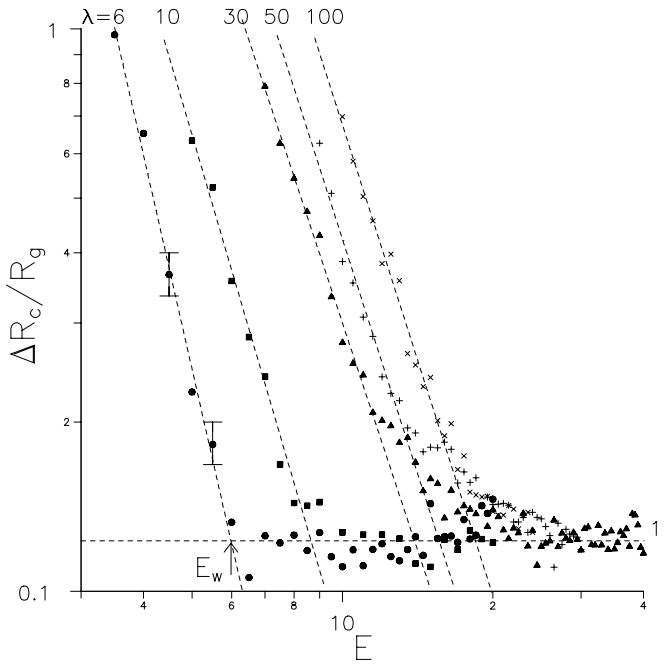

Fig. 8. The $\Delta R_c/R_g$, *versus* E dependencies at different values of λ. Here, ΔR_c is the root-mean-square averaged distance between the initial seed point and the centre of mass of the cluster, and R_g is gyration radius of cluster. Each point is obtained by averaging over the 100–200 different runs. The value of E_w for given a λ can be determined as an intersection point of large-E asymptotic line 1 and corresponding small–E asymptotic dashed line, as it is shown for $\lambda = 6$

Figure 7 presents the large scale patterns (a) and interface evolution time snapshots (b) for the$\mathbf{W}_\infty$-cluster and $\mathbf{DB}_\infty$-cluster at $\lambda = 30$ and for the $E = 9$ and $E = 14$, respectively. These are the same clusters as those shown as 10 and 11 in Figure 1, but they were grown at the larger scale lattice of 4000×4000 dimension. Here, for the $\mathbf{W}_\infty$ worm-like cluster, the time snapshots show the strong interface fluctuations and a large surface width of the growth front, which can considerably deviate from the circular form. For the **DB**-cluster, we observe almost circular growth of interface with a small surface width. The strong fluctuations observed for the worm-like clusters can be explained by the fact that in this case the newcomer particles can join the cluster in its deep interior. For the **DB**-clusters, the newcomer particles join mostly on the outer near-circular boundary.

Such differences in the character of cluster growth provide us with the easy way of visual localisation of the boundary between the $\mathbf{W}_\infty - \mathbf{DB}_\infty$ or $\mathbf{W_f} - \mathbf{DB_f}$ regions. But visual method is not very accurate and for the quantitative purposes we analysed the $\Delta R_c/R_g$ value, where ΔR_c is the root-mean-square averaged distance between initial seed point and the centre of mass of the cluster (centre of mass displacement), and R_g is gyration radius of cluster. Figure 8 presents the example of $\Delta R_c/R_g$ *versus* E dependencies for fixed $N = 1000$ at different λ, and we localise the transition value E_w by the intersection point of small-E and large-E asymptotics as displayed by the dashed lines. The values of E_w given by this method confirm the data of visual analysis as described above.

Note that near the $\mathbf{W}_\infty - \mathbf{DB}_\infty$ or $\mathbf{W_f} - \mathbf{DB_f}$ boundaries we observe approximately the same fractions of particles in configurations of (2), (3) and (4) types ($P_2 \approx P_3 \approx P_4 \approx 0.2$–$0.3$), and in all the cases the maximum point of P_1 is localised near the $E \approx E_w$ (see Figs. 4a–5a). At further E increase in the range of region $\mathbf{DB}_{\infty(\mathbf{f})}$, we observe the increase of P_4 and decrease of P_{1-3}, that, of course, reflects the fact of increase of the radius of cluster dense part, R_c.

3.3 Radial structure of cluster

The mechanisms of the internal cluster structure formation, as well as the matters dealing with its morphology may be clarified by the analysis of changes of certain cluster properties in the radial direction. For this purpose, we have analysed the local density profiles $\rho(r)$ and the $E/U(r)$ ratio that characterise both the cluster growth

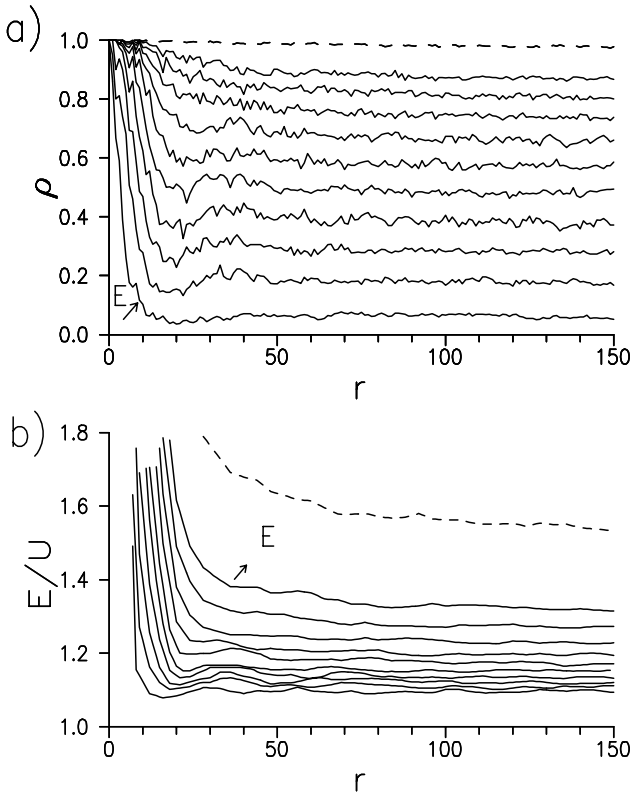

Fig. 9. The radial profiles of local cluster density, $\rho(r)$, and the energy ratios, $E/U(r)$. The results correspond to the different values of attraction energy $E = 10, 20, 30, 40, 50, 60, 70, 80, 90, 100$ (solid lines), $E = 130$ (dashed line), the arrow shows the direction of E increase. The screening length is $\lambda = 30$.

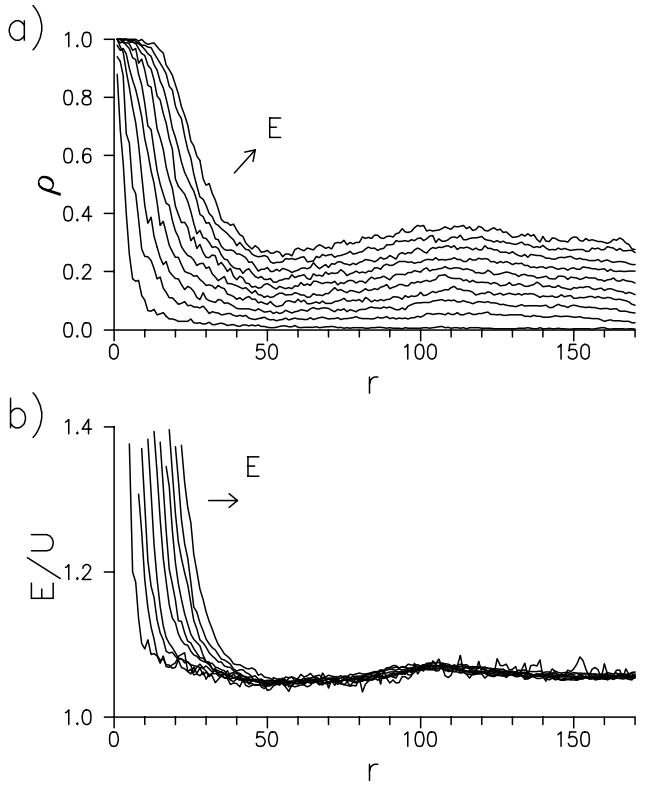

Fig. 10. The radial profiles of local cluster density, $\rho(r)$, and the energy ratios, $E/U(r)$. The results correspond to the different values of attraction energy $E = 10, 20, 30, 40, 50, 60, 70, 80, 90, 100$ (solid lines), $E = 200(1), 300(2)$ (dashed lines), the arrow shows the direction of E increase. The screening length is $\lambda = 100$.

stability and the possibility of cluster growth termination if the condition (2) is realised.

We define the local density profile as

$$\rho(r) = N(r)/N_{\rm c}(r), \tag{15}$$

where $N(r)$ is the number of cluster particles inside a ring of radius r and one lattice unit width, centred at a seed particle; $N_{\rm c}(r)$ is the similar number of densely packed cluster particles. This definition implies that the denser is the cluster, the closer is its density to 1.

Consequently, according to this definition, the value of ρ corresponds to the relative density profile reduced to a density profile of densely packed cluster. This definition allowed us to suppress the long-range effects of magic numbers, that are clearly present in the density profiles of densely packed clusters on regular lattices [23].

Figures 9–11 present the profiles of local density, ρ (a) and E/U (b) for clusters obtained at $\lambda = 30, 100$ and ∞, respectively. These dependencies were obtained at $E = 10, 20, ..., 100$ for each λ and averaged over 10 clusters grown on 400×400 lattice (for $\lambda = 30, 100$) and 300×300 lattice (for $\lambda = \infty$). Thus, we have analysed the structure of clusters in the following regions: $\mathbf{W}_\infty, \mathbf{DB}_\infty$ and $\mathbf{C}_\infty$ (for $\lambda = 30$), $\mathbf{W}_\infty$ and $\mathbf{DB}_\infty$ (for $\lambda = 100$), as well as the regions $\mathbf{W_f}$ and $\mathbf{DB_f}$ (for $\lambda = \infty$) (see the phase diagram in Fig. 2).

In all the cases we have observed a rather sharp and mutually-correlated initial decrease of ρ and E/U values with r increase. For $\lambda = 30$ and $\lambda = 100$ in $\mathbf{DB}_\infty$ region these dependencies have minimum at $r \approx \lambda/2$ and maximum at $r \approx \lambda$. Analysis of the $\rho(r)$ and $E/U(r)$ profiles allows us to make some general conclusions dealing with the character of internal cluster structure inhomogeneity. In general case, four different zones of spatial cluster structure in $\mathbf{DB}_\infty$ region may be discerned along the radial direction of cluster structure (Fig.12):

- zone **A** or internal compact nucleus; this nucleus zone has the density of $\rho \approx 1.0$ and its radius may be estimated as $R_{\rm n} \approx E/4$ (See Appendix, Eq. (A.5)); it results from the simple Eden-like growth terminated when condition (2) fulfils for the first time

- zone **B** or near-nucleus boundary ring; this low density ring is located in the region of $R_{\rm n} < r < \lambda/2$; here, each newly attached particle "feels" repulsion of all the particles of a cluster; the formation of this ring begins when some of perimeter sites on the cluster exterior cannot be filled because of condition (2) and the growth of near-linear branches directed outward from the dense

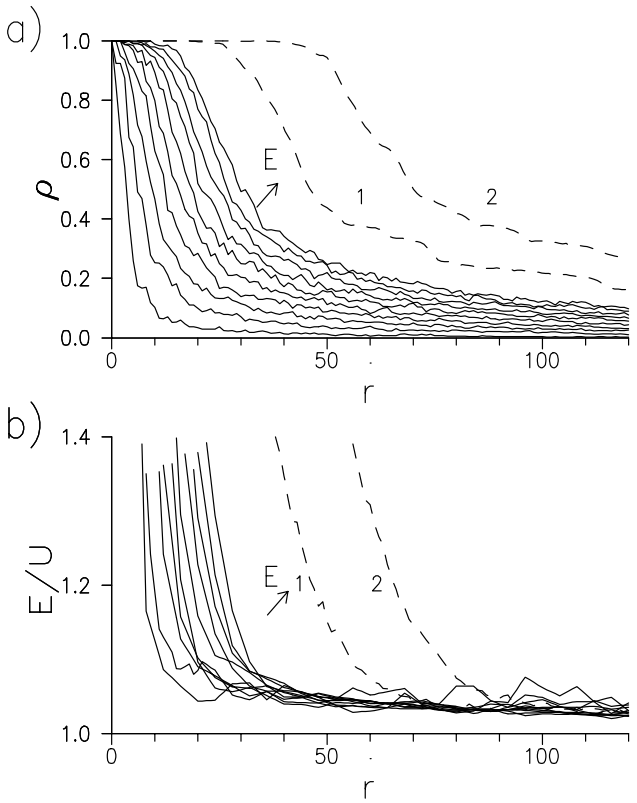

Fig. 11. The radial profiles of local cluster density, $\rho(r)$, and the energy ratios, $E/U(r)$. The results correspond to the different values of attraction energy $E = 10, 20, 30, 40, 50, 60, 70, 80, 90, 100$ (solid lines), $E = 200(1), 300(2)$ (dashed lines), the arrow shows the direction of E increase. The screening length is $\lambda = \infty$.

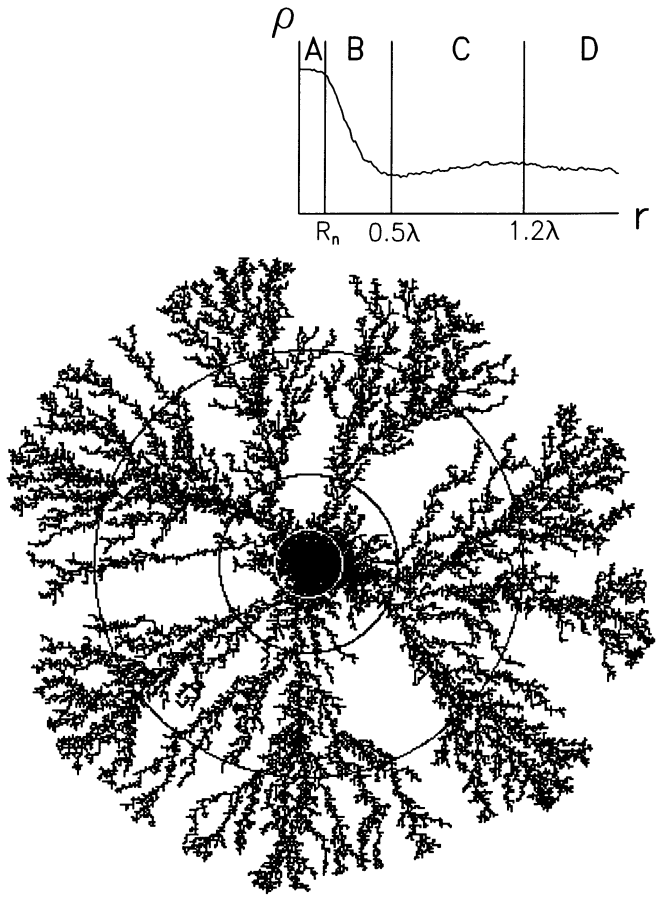

Fig. 12. The scheme of the internal structure of cluster in $\mathbf{DB}_\infty$ region. We display the example of cluster pattern and its local density profiles $\rho(r)$ in radial direction. The intervals of localisation of different zones $\mathbf{A}, \mathbf{B}, \mathbf{C}$ and $\mathbf{D}$ are shown, R_n is the compact nucleus radius, λ is the screening length.

nucleus is observed; the local density of the clusters drops in this zone, approximately as $\rho \propto 1/r$ in all the cases investigated;

- zone **C**, or screening-induced compression ring; this zone is located in the region of $\lambda/2 < r < 1.2\ \lambda$ and may occur only for finite λ's; in this zone, each newly attached particle does not "feel" repulsion from all the particles of a cluster but only from those particles that are localised at distances shorter than the screening length λ; when $r > \lambda - R_\mathrm{n} \approx \lambda - E/4$, this screening includes the particles of the most dense part of a cluster (its nucleus) and, as a result, the partial increase of density (or compression) with r increase is observed; the density maximum (see Figs. 9a–10a) and, correspondingly, the maximum of the $E/U(r)$ is observed at $r \approx \lambda$ (see Figs. 9b–10b);

- zone **D**, or external zone; finally, at large $r > 1.2\ \lambda$ the influence of the core region disappears and growth regime becomes asymptotic.

For the case of $\lambda = 30$ (Fig. 9), the energy, E, increase from 10 to 100 corresponds to the gradual transition $\mathbf{W}_\infty \to \mathbf{DB}_\infty \to \mathbf{C}_\infty$ on the phase diagram. At $E = 10$ (the lowest curve), we are near the border of $\mathbf{W}_\infty \to \mathbf{DB}_\infty$ (for example, see Fig. 1, cluster 10 ($E = 9$)). The zone **A** is absent in this case, since the nucleus radius is very small ($R_\mathrm{n} \approx E/4 = 2.5$). At $20 < E < 80$, we are in $\mathbf{DB}_\infty$ region (for example, see Fig. 1, cluster 12($E = 20$)); here, each energy, E, increase by 10 results in a nucleus radius increase, approximately, by 2.5. In this case, the profiles of $\rho(r)$ and $E/U(r)$ reveal somewhat nontrivial behaviour, and we can find the zones **A** – **D** in the cluster structure. At $E \geq 80$, we are almost near the border of $\mathbf{C}_\infty$ region. We observe that $\rho(r)$ and $E/U(r)$ profiles get elevated with E increase; these profiles decrease with r without passing through maxima and minima. The dashed lines in Figure 9 correspond to the case of $E = 130$, *i.e.*, when we are far in the $\mathbf{C}_\infty$ region, where the clusters are densely packed or compact. In this last case, $\rho(r) \approx 1.0$ is observed and the different zones of cluster structure may be discerned only by the character of $E/U(r)$ decrease.

The similar behaviour of $\rho(r)$ and $E/U(r)$ profiles is observed also in the case of $\lambda = 100$ (Fig. 10). However, some aspects of the cluster structure are more explicit in this case. Here, we have the more prominent maxima and minima of $\rho(r)$ and $E/U(r)$ profiles, and we observe no general elevation of $E/U(r)$ curves with E increase. It may be explained by the fact that this behaviour is pronounced only at sufficiently large values of E in the proximity of compact growth region $\mathbf{C}_\infty$. We had not reached

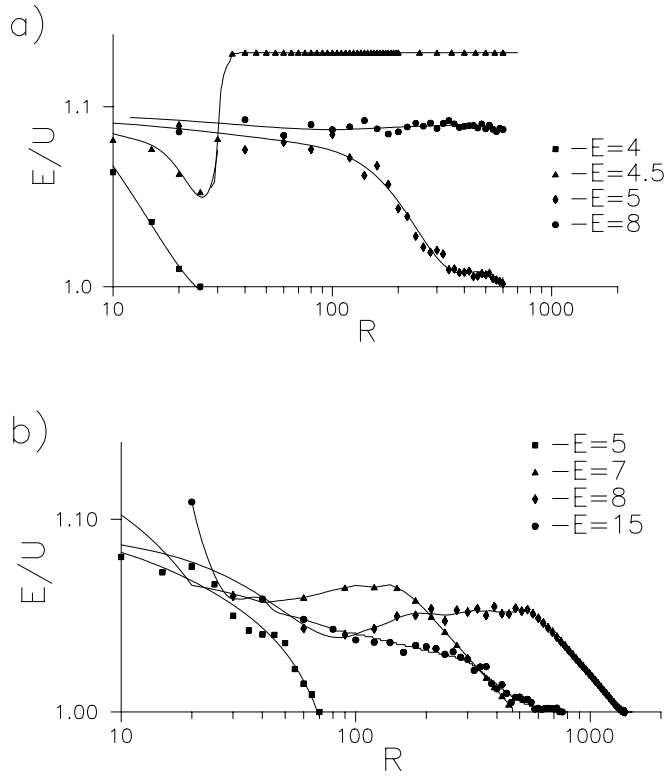

Fig. 13. The radial profiles of the energy ratios, $E/U(r)$, for the screening length $\lambda = 30$(a), ∞(b).

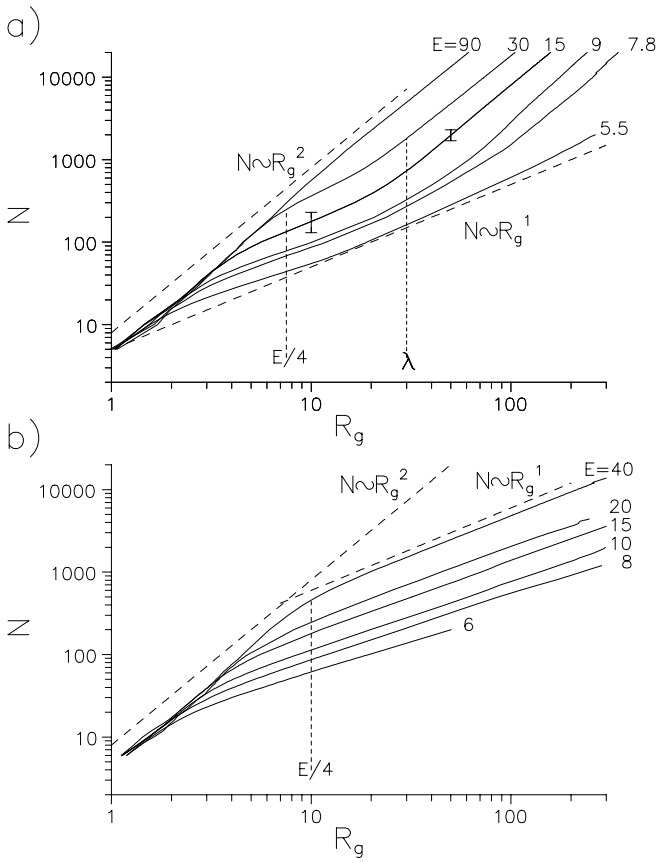

Fig. 14. Log–log plot of the number of particles in the cluster, N, *versus* its radius of gyration, $R_{\rm g}$, at $\lambda = 30$ (a), $\lambda = \infty$ (a) and different E. The results are averaged over 50 clusters for each value of E. The inclined dashed lines correspond to the slopes $D_{\rm f} = 2$ and $D_{\rm f} = 1$, respectively. The vertical dashed lines show the values of $R_{\rm g} = E/4$ for $E = 30$(a) and for $E = 40$(b), and the value $R_{\rm g} = \lambda = 30$(a)

$\mathbf{C}_\infty$ region in our simulations: for $\lambda = 100$, it starts only at $E \geq 300$.

At $\lambda = \infty$, the profiles of $\rho(r)$ and $E/U(r)$ (Fig. 11) do not pass through maxima and minima, but simply drop almost like $1/r$ outside the nucleus zone, **A**. Figures 1 (patterns 21–24) contain good examples of such clusters. The dashed lines (Fig. 12) correspond to the cases when $E = 200(1)$ and $300(2)$. In these cases, the clusters have the large compact nuclei with the radii of $R_{\rm n} \approx 50$–75.

We have also analysed the behaviour of the $E/U(r)$ profiles for sufficiently small values of E in regions $\mathbf{L_f}$, $\mathbf{Lb}_\infty$ and $\mathbf{W_f}$ for $\lambda = 30$ (Fig. 13a) and in regions $\mathbf{L_f}$, $\mathbf{Lb_f}$ and $\mathbf{W_f}$ for $\lambda = \infty$ (Fig. 13b). Each of these $E/U(r)$ profiles was obtained through data averaging over the 10 different clusters. In the regions of finite cluster growth, the $E/U(r)$ decreases quickly with r upraise. At certain critical value of $r = R_{\rm max}$, we observe $E/U(r) \leq 1$ at all the points of cluster perimeter and just at this stage the cluster stops to grow. In transition zone between the finite and infinite growth regions, $E/U(r)$ takes a certain stationary value greater than 1.

Remarkable is the case of $\lambda = 30$ and $E = 4.5$ (Fig. 13a), when we get into the narrow $\mathbf{Lb}_\infty$ region on the phase diagram of Figure 2. We see that after the fast initial decrease of $E/U(r)$, its abrupt upraise is observed at certain $r \approx \lambda$, and then the value of $E/U(r)$ does not change with r. This condition corresponds to formation of the infinite linear clusters or linear clusters with bending.

3.4 Scaling properties of clusters

As we have shown in the previous Section 3.3, in the general case, the clusters obtained within our model do not reveal any homogeneous properties in their radial direction. Therefore, the fractal approach is not applicable for analysis of the structure of a whole cluster, and we do not expect to see any universal power law relation between the number of particles in the cluster N and its radius of gyration $R_{\rm g}$, such as

$$N \propto R_{\rm g}^{D_{\rm f}}, \tag{16}$$

where $D_{\rm f}$ is the scaling exponent, or, for the self–similar objects, is their fractal dimensionality.

Nevertheless, we have analysed the scaling properties of clusters through investigation of the log–log plots of N *versus* $R_{\rm g}$ as presented in Figures 14a and 14b for $\lambda = 30$ and $\lambda = \infty$, respectively. For all the λ's, the gradually curved data in the crossovers between different scaling regimes are observed. At $R_{\rm g} \leq R_{\rm n} \approx E/4$ the scaling

regime with the exponent $D_f \approx 2$ in equation (16) corresponds to the compact cluster growth. At $\lambda = \infty$, the $R_g \to \infty$ asymptotic regime is characterised by the exponent $D_f \approx 1$ and this non–fractal behaviour is easy to understand in view of the tendency of electrostatic repulsion to linearise the branches of the cluster.

For the case of finite λ (Fig. 14a), the $R_g \to \infty$ asymptotic regime in the infinite phases $\mathbf{W}_\infty$, $\mathbf{DB}_\infty$ and $\mathbf{C}_\infty$ is characterised by another limiting exponent $D_f \approx 2$ in equation (16). This behaviour corresponds to the non–fractal uniform filling of the 2d–space.

At $E > E_w = E_{\mathbf{W}_\infty - \mathbf{DB}_\infty(\mathbf{W_f} - \mathbf{DB_f})}$, the crossover region, where the effective value of D_f is closer to 1 is localised approximately at the interval of $E/4 \lesssim R_g \lesssim \lambda$. The detailed analysis shows that for the small values $E < E_w$, the crossover region may be far more extended and in finite phases at $E < E_{\mathbf{W_f}-\mathbf{W}_\infty}$ (in the phases $\mathbf{W_f}$ and $\mathbf{L_f}$) the effective scaling exponent D_f in the region $R_g > E/4$ is practically always equal to 1.

We should stress here that within our stochastic model the exponent $D_f = 1$ is observed also in the reentrant infinite phase $\mathbf{Lb}_\infty$. Somewhat different scaling behaviour is observed for the deterministic model of charged particles aggregation, where the sharp transition between $D_f = 1$ for finite and $D_f = 2$ for infinite clusters exists [25].

4 Conclusions

We have introduced the two–parametric electrostatic Eden model that simulates the aggregation of charged particles. Cluster growth is controlled by the screening length of electrostatic interactions λ, and the energy of particle adhesion to a cluster E. The phase diagram in λ *versus* E co–ordinates reveals the regions of *finite* (f) and of *infinite* (∞) cluster growth. The model gives a variety of patterns with different morphology. We do discern the following morphologic types: linear, linear with bending, worm–like, dense–branching and compact Eden–like. The structure compactness increases with the attraction energy E increase, while the strengthening of electrostatic repulsion on λ increase results in linear morphologies predominance. The cluster structure is not homogeneous in the radial direction and in the general case four zones with different morphological properties may be differentiated: internal compact nucleus zone, near–nucleus boundary ring, screening induced compression ring, and external ring.

Appendix A: Simple electrostatic estimations for the model

We approximate a compact two–dimensional Eden cluster by uniformly charged disk of radius R. We calculate the energy of electrostatic interaction between the charge and compact disk–like cluster of charged particles U by using numerical integration instead of summation in equation (1) and taking into account the homogeneous charge density distribution in the disk–like cluster with $\rho(r) = 1$.

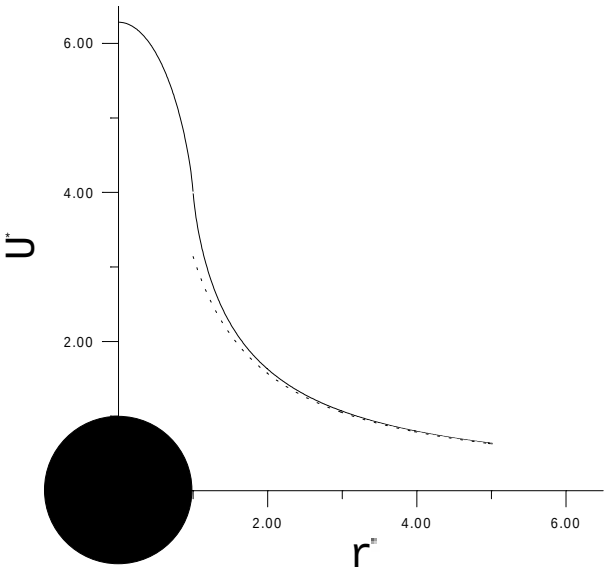

Fig. 15. The reduced electrostatic interaction energy $U^* = U/R$ *versus* the reduced distance between the centre of compact disk–like cluster and unit charge, $r^* = r/R$ at the screening length $\lambda = \infty$. Here R is the radius of the charged disk.

The solid line in Figure 15 presents the dependency of the reduced electrostatic energy, $U^* = U/R$, against the reduced distance between the charge and the cluster centre, $r^* = r/R$, for $\lambda = \infty$. It is obvious that for the particle located at the cluster centre, when $r = 0$, the energy is equal to $U_o = 2\pi R$. At large distances from the cluster centre, when $r^* \to \infty$, we may neglect the spatial charge distribution inside the cluster and treat the whole charged cluster as a charge $Q = \pi R^2$ concentrated at the centre of this cluster. In this case:

$$U^*(r^* \to \infty) = U^*_\infty = \pi / r^*. \tag{A.1}$$

The dependency of U^*_∞ on r^* is presented in Figure 15 by the dashed line. We see, that, at least, for $r^* > 1.5$, the equation (A.1) approximates the $U^*(r^*)$ dependency rather precisely.

If the particle is located at the circle–like cluster perimeter, where $r = R$ ($r^* = 1$), the interaction energy expressions are easy to obtain in the analytical form for the arbitrary λ value:

$$U^*_p = 4(1 + \lambda^* \arccos(\lambda^*) - \sqrt{1 - \lambda^{*2}}) \text{ for } \lambda^* < 1 \tag{A.2}$$

$$U^*_p = 4 \text{ for } \lambda^* \geq 1. \tag{A.3}$$

Here, $\lambda^* = \lambda/(2R)$.

The condition $\lambda^* \geq 1$ from equation (A.3) is equivalent to the condition $\lambda \geq 2R$. In this case, the U_p value is defined by the interactions with all the cluster charges, without any screening limitations. Thus, for all the $R \leq \lambda/2$, we obtain from equation (A.3):

$$U_p = 4R. \tag{A.4}$$

The stable growth of compact aggregates terminates when $E \leq U_{\rm p}$; therefore, in the specific case of $\lambda = \infty$ we may estimate the radius of the compact nucleus as

$$R_n \approx E/4, \text{for } \lambda = \infty. \quad \text{(A.5)}$$

At $R \geq R_{\rm n}$, the loss of compact cluster growth stability takes place and cluster ramification begins.

It is possible to estimate the $R_{\rm n}$ values for finite screening lengths, λ's, by substituting $U_{\rm p} = E$ into equation (A.2). However, in this case the situation of an infinite compact cluster growth with $R_{\rm n} = \infty$ is possible for sufficiently large values of $E \geq E_{\rm c}$. For the purposes of $E_{\rm c}$ estimation, we consider equation (A.2) when $\lambda^* \to 0$ (or $R \to \infty$ when λ is a finite) and obtain $U_{\rm p}^* = 2\pi\lambda^*$ or $U_{\rm p} = \pi\lambda$. So, the relation for $E_{\rm c}(\lambda)$ may be written as follows:

$$E_{\rm c}(\lambda) = \pi\lambda. \quad \text{(A.6)}$$

Equation (A.6) allows us to estimate the position of the boundary between the $\mathbf{C}_\infty$ and $\mathbf{DB}_\infty$ regions on the phase diagram presented in Figure 2.

Authors thank Dr. N.S. Pivovarova for valuable discussions of the manuscript and help with its preparation.

References

1. *Kinetics of Aggregation and Gelation*, edited by F. Family, D.P. Landau (Noth-Holland, Amsterdam, 1984); P. Meakin, in *Phase Transition and Critical Phenomena*, edited by C. Domb, J.L. Lebowitz (Academic Press, London, 1988), Vol. 12, p. 335; T. Vicsek, *Fractal Growth Phenomena* (World Scientific, Singapore, 1989); M. Mutsushita, in *The Fractal Approach to Heterogeneous Chemistry*, edited by D. Avnir (Wiley, Chichester, 1990), p. 161.
2. M. Eden, in *Proceedings of the Fourth Berkeley Symposium on Mathematics, Statistics and Probability, 1961*, edited by F. Neyman (University of California Press, Berkeley, 1961), Vol. 4, p. 223.
3. T.A. Witten, L.M. Sander, Phys. Rev. Lett. **47** 1400 (1981).
4. Z.Q. Wu, B.Q. Li, Phys. Rev. E **51**, R16 (1995); B. Li, J. Wang, B. Wang, W. Liu, Z. Wu, Europhys. Lett. **30**, 239 (1995).
5. G.C. John, V.A. Singh, Phys. Rev. E **53**, 3920 (1996).
6. W. Huang, D.B. Hibbert, Phys. Rev. E, **53**, 727 (1996).
7. J. Elebacher, P.C.Searson, K. Sieradski, Phys. Rev. Lett. **71**, (20) 3311 (1993).
8. N. Nagatani, F. Sagués, J. Phys. Soc. Jpn. **59**, 3447 (1990); E. Ben-Jacob, H. Shmueli, O. Shochet, A. Tenenhaum, Physica A, **187**, 378 (1992); I. Mogi, S. Okubo, G. Kido, Fractals **1**, 475 (1993); S. Fautrat, P. Mills, Phys. Rev. E **53**, 4990 (1996).
9. H. Fujikawa, M. Matsushita. J. Phys. Soc. Jap. **58**, 3875 (1989); E. Ben-Jacob, I. Cohen, O. Shochet, I. Aronson, H. Levine, L. Tsimering, Nature **373**, 566 (1995); Y. Kozlovsky, I. Cohen, I. Golding, E. Ben-Jacob, Phys. Rev. E **59**, 7025 (1999).
10. P.A. Rikvold, Phys. Rev. A **26**, 674 (1982); P. Meakin, Phys. Rev. Lett. **51**, 1119 (1983); P. Meakin, Phys. Lett. A **107**, 269 (1985).
11. M. Ausloos, N. Vandewalle, R. Cloots, Europhys. Lett. **24**, 629 (1993).
12. N. Vandewalle, M. Ausloos, Phys. Rev. E **51**, 597 (1995).
13. P.M. Mors, R. Botet, R. Jullien, J. Phys. A: Math. Gen. **20**, L975 (1987); R. Pastor-Satorras, J.M. Rubi, Phys. Rev. E **51**, 5994 (1995).
14. G.A. Helgessen, A.T. Skjeltorp, P.M. Mors, R. Botet, R. Jullien, Phys. Rev. Lett. **61**, 1736 (1988); G. A. Niklasson, A. Torebring, C. Larsson, C.G. Granqvist, Phys. Rev. Lett. **60**, 1735 (1988).
15. A. Fernández-Barbero, M. Cabrerizo-Vilchez, R. Martinez-Garcia, R. Hidalgo-Alvarez, Phys. Rev. E **53**, 4981 (1996).
16. J.-N. Chazalviel, Phys. Rev. A **42**, 7355 (1990).
17. W. Breazeal, K.M. Flynn, E.G. Gwinn, Phys. Rev. E **52**, 1503 (1995).
18. B.W. Smirnov, Phys. Rep. **152**, 177 (1987).
19. H. Gao, Z. Xue, Q. Wu, S. Pang, J. Mater. Res. **9**, 2216 (1994); H. Gao, Z. Xue, Q. Wu, S. Pang, Solid State Comm. **97**, 579 (1996); I.M. Sandler, G.S. Canright, H. Gao, S. Pang, Z. Xue, Z. Zhang, cond-mat/9809198 (1998) (preprint).
20. L.D. Landau, E.M. Lifshitz *Electrodynamics of Continuous Media* (Nauka, Moscow, 1982).
21. Y. Kantor, M. Kardar, Phys. Rev. E **51**, 1299 (1995).
22. P.C. Reist *Introduction to Aerosol Science* (Macmillan, New York, 1984).
23. B.W. Smirnov, *Cluster Ions and van der Waals Molecules* (Gordon and Breach, London, 1991).
24. *Handbook of Mathematical Function with formulas, Graphs Mathemathical Tables*, edited by M. Abramowitz, I.A. Stegun (National Bureau of Standards Applied Mathematics Series 55, New York, 1964).
25. N.I. Lebovka, Ya.V. Ivanenko, N.V. Vygornitskii, Europhys. Lett. **41**, 19 (1998).